Evolution of the Optical Functions of Aluminum Films during Nucleation and Growth Determined by Real-Time Spectroscopic Ellipsometry

H. V. Nguyen, Ilsin An, and R. W. Collins
Department of Physics and Materials Research Laboratory, The Pennsylvania State University, University Park, Pennsylvania 16802
(Received 13 September 1991)

We report the first measurements of the optical functions of polycrystalline metal films throughout nucleation and growth. The dielectric function of aluminum, evaporated onto SiO_2, was determined versus thickness d by real-time multichannel ellipsometry ($1.3 \leq h\nu \leq 4.1$ eV). We find that the electron relaxation time for the (200) parallel-band transition is independent of particle size during nucleation ($d < 50$ Å) and increases abruptly only after coalescence. This behavior is not consistent with a classical size effect and suggests that the atomic structure of the particles dominates their optical properties.

PACS numbers: 78.65.Ez, 07.60.Fs, 68.55.Jk, 73.60.Aq

The influence of microstructure on the optical properties of very thin metal films has been studied extensively since Maxwell-Garnett (MG) explained the observed optical absorption (or plasmon-polariton) band with a model of the film as a slab of dispersed particles interacting according to the Lorentz local-field description [1,2]. More recently, quantitative analysis of metal particle films by electron microscopy has provided input to an extended MG effective-medium theory (EMT) that includes dipole-dipole interactions among ellipsoidal particles and size-dependent optical functions, in attempts to simulate transmittance (T) spectra [3].

In the film growth regime when metal particles begin to coalesce, the microstructure also strongly affects the optical properties [4]. Among classical EMTs, only that of Bruggeman [5] predicts a transition between dielectric and metallic optical behavior. Scaling concepts are required near the percolation threshold, explaining observed wavelength-independent T spectra in the near-infrared region [6]. For continuous metal films, an improved understanding of the optical properties has resulted from the development of methods for interpreting ellipsometric spectra [7]. These employ the Bruggeman EMT and linear regression analysis (LRA) to deduce quantitative information: relative bulk void volume fractions, surface roughness thicknesses, along with their confidence limits [8].

Here we employ rapid-scan spectroscopic ellipsometry (SE) to obtain, for the first time, the evolution of the optical functions during metal film deposition, spanning the regimes of nucleation, coalescence, and bulk film growth. A near-century of experience on metals is applied to deduce electronic and microstructural information solely from SE. This is an important goal because the real-time optical probe, in contrast to direct probes of microstructure, is noninvasive and requires no *in vacuo* equipment. In addition, through rigorous LRA, we seek to establish the minimum theoretical input needed to understand the evolving thin-film optical functions. For our first such study, Al was chosen because its optical functions can be expressed in terms of photon-energy-independent parameters using the Ashcroft and Sturm formulas (AS) [9].

Al was evaporated from a W filament onto thermally oxidized c-Si substrates at 25 °C. Real-time SE results will be presented for two depositions with rates of 280 and 43 Å/min. The lower rate led to a lower nucleation density, permitting study of the particle growth regime over a wider thickness range. The pressure-to-rate ratios were $\sim 10^{-9}$ Torr min/Å in each case, ensuring negligible contamination at least with respect to the optical properties [10]. After deposition (and real-time SE), the high-rate Al film was dissolved in dilute HCl, and the exposed substrate surface was studied by *ex situ* SE. The finding that the substrate optical properties were unchanged by Al deposition indicates the absence of a SiO_2/Al interfacial reaction, even at the monolayer level.

Details of our rotating polarizer multichannel ellipsometer appear elsewhere [11]. With this instrument, 85-point (ψ,Δ) spectra can be collected from 1.3 to 4.1 eV in an optical cycle of 40 ms. (ψ,Δ) are defined by $\tan\psi \exp(i\Delta) = r_p/r_s$, where r_p and r_s are the complex reflection coefficients for p and s waves. At least eight optical cycles of data accumulation (0.3 s) are needed for monolayer sensitivity to film thickness, and for the high- (low-) rate Al deposition the repetition period was set at 1.3 s (5.5 s). The angle of incidence was 70° for all measurements.

First we needed to ensure that the final real-time (ψ,Δ) spectra for the opaque Al film obtained after ~ 3 min of high-rate deposition (~ 800 Å) were consistent with previous results. Thus, we applied LRA to these spectra using a three-medium (ambient/roughness/bulk) model, the Bruggeman EMT, and the most widely accepted dielectric function for Al [12]. The following information was deduced: bulk and roughness layer void fractions, 0.001 ± 0.005 and 0.51 ± 0.02; and roughness layer thickness, 10.5 ± 0.5 Å. Because our final film has an identical bulk void fraction as the Al of Ref. [12], both most likely exhibit single-crystal density.

The roughness was analytically removed from the final spectra to obtain the bulk dielectric function ε_b of our Al.

This was interpreted by LRA using the AS formulas, expressed formally as

$$\varepsilon_{AS}(\omega)=1+\frac{4\pi i\sigma_a}{\omega}\left[\frac{32a_0k_F(\varepsilon_F\tau_D/h)}{(m_{opt}/m_e)(1-i\omega\tau_D)}+\sum_K(a_0K)J_K(\omega,|U_K|,\tau_K)\right], \quad (1)$$

including the Drude term and two parallel-band terms, J_{200} and J_{111}, for transitions associated with the (200) and (111) zone faces [9]. The following were fixed in all LRAs employing Eq. (1): Fermi wave vector, $k_F=1.749$ Å^{-1}; coefficient of the crystal potential, $|U_{111}|=0.25$ eV; and Drude optical mass, $m_{opt}/m_e=1.55$ [9,13]. In the LRA of ε_b, we also fixed the Drude relaxation time τ_D at the literature bulk value, $\tau_{D,b}=10.6\times10^{-15}$ s, and equated the bulk (200) and (111) relaxation times, $\tau_{200,b}=\tau_{111,b}\equiv\tau_{PB,b}$, owing to an insensitivity to the Drude and (111) contributions above 1.3 eV. A good fit to ε_b was obtained for $|U_{200}|=0.73$ eV and $\tau_{PB,b}=4.1\times10^{-15}$ s in agreement with Ref. [13].

We next extracted the dielectric function, $\varepsilon=\varepsilon_1+i\varepsilon_2$, from the real-time SE data in the earlier growth stages using a one-layer, isotropic model for the Al. This analysis was performed by selecting the Al thickness to minimize c-Si substrate artifacts in $(\varepsilon_1,\varepsilon_2)$, obtained by inversion from (ψ,Δ) [14]. The fact that the artifacts could be eliminated indicates that the one-layer model is realistic. In addition, we demonstrate below that the assumption of isotropy is also valid.

Selected $(\varepsilon_1,\varepsilon_2)$ for the high-rate Al deposition appear in Fig. 1 for comparison. The 23-Å result features a plasmon-polariton band near 3.4 eV and is consistent with isolated particles. The percolation threshold occurs between 44 and 53 Å, and ε_1 drops to negative values in the near-infrared region. Although the metallic optical behavior at 53 Å is indicative of a continuous film, there is no evidence of the 1.5-eV (200) parallel-band feature in ε_2. This feature develops between 53 and 61 Å (see Fig. 1), and dominates ε_2 for the thicker 106-Å film. In the following, we will first describe an LRA of the (ψ,Δ) spectra in the continuous film regime (>50 Å) for the high-rate Al. Then, we will concentrate on an analysis of $(\varepsilon_1,\varepsilon_2)$ in the particle regime for the low-rate Al.

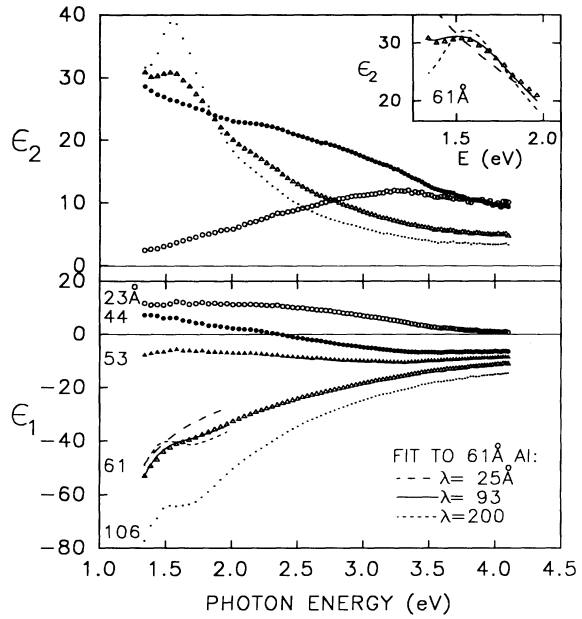

FIG. 1. Selected dielectric functions obtained from real-time SE of Al film growth (280 Å/min) determined according to an isotropic, one-layer model for the Al. Simulations of the results for the 61-Å film using a variable mean free path λ are included (inset for ε_2).

In the LRA of the high-rate Al spectra for $d>50$ Å, the AS formulas were applied as above. The (200) and (111) parallel-band relaxation times were equated, and all τ_j in Eq. (1) were related to a mean free path λ and the known bulk values $\tau_{j,b}$ through $\tau_j^{-1}=\tau_{j,b}^{-1}+v_F/\lambda$, where v_F is the Fermi velocity [15]. λ (and τ_j) in very thin films is a sensitive function of boundary and defect scattering. Other parameters in Eq. (1) were fixed at values given earlier. In addition, we attempted to include possible changes in microstructure in the LRA, modeled with the Bruggeman EMT. A 10-Å stable surface roughness layer provided a minor improvement in the fits; no improvement was obtained, however, for $d>50$ Å by incorporating a variable void volume fraction. In fact, a close fit to the (ψ,Δ) spectra for the $d<60$ Å range was possible only by applying size-modified Al optical functions. Comparison between the simulations (best fit for $\lambda=93$ Å) and $(\varepsilon_1,\varepsilon_2)$ data near the (200) parallel-band transition are shown in Fig. 1 for the 61-Å film (see inset for ε_2).

In Fig. 2 the final LRA results for τ_{PB} and λ are presented versus total thickness d for the high-rate Al (triangles, $d>50$ Å). A remarkable effect is observed: λ (τ_{PB}) increases by a factor of 10 (5) for $55<d<60$ Å. We ascribe this transition to the healing or crystallization of nucleation-induced, defective or disordered domains having insufficient (200) translational symmetry for the development of the parallel-band feature. For $d>60$ Å, λ and τ_{PB} increase gradually with d owing to a reduction in grain boundary scattering as the grain radius R_g increases. In this model, $\lambda\sim2[(1-\Re)/3\Re]R_g$, where $\Re$ is the grain boundary reflection coefficient [16,17]. If $R_g=2.5(d/2)$ (see below), then a good fit to the data for $d>60$ Å is obtained for $\Re=0.30$ (solid line in Fig. 2), in comparison with an earlier result of 0.15 from electrical resistivity measurements [16].

Next, the particle growth regime will be studied for the low-rate Al. This regime is evident in the first ~50 Å, as shown by $(\varepsilon_1,\varepsilon_2)$ of Fig. 3, extracted using a single-film, isotropic model. We have considered these results within

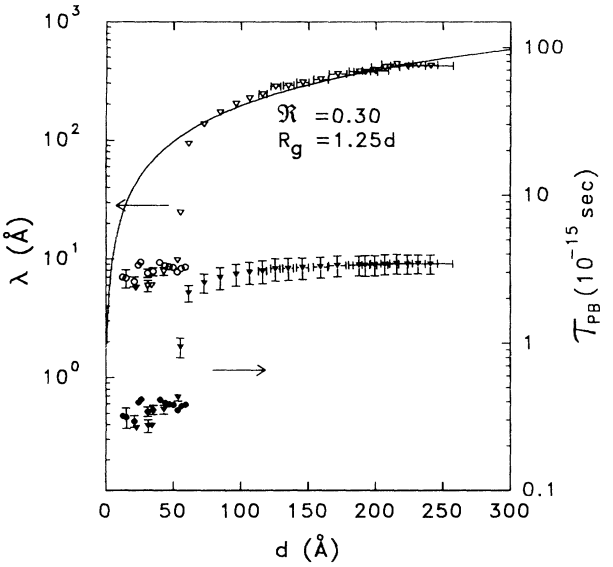

FIG. 2. Electron mean free path (open points) and parallel-band relaxation time (solid points) as a function of thickness for two Al films (triangles: 280 Å/min; circles: 43 Å/min). The triangles for $d > 50$ Å were deduced from a bulk microstructural model; all other data were deduced from the extended MG EMT [Eqs. (2)]. The error bars are the confidence limits. The solid line is a fit to λ for $d > 60$ Å for a grain growth model.

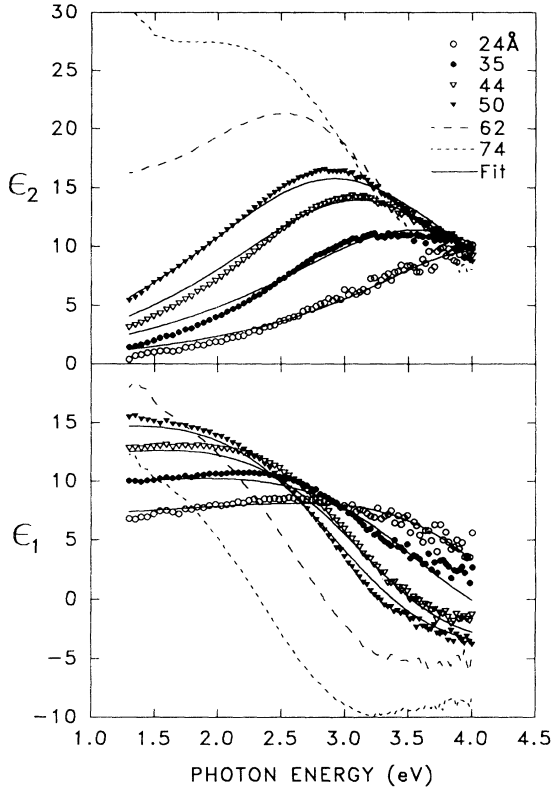

FIG. 3. Selected dielectric functions obtained from real-time observations of Al film growth (43 Å/min) determined according to an isotropic, one-layer model. The solid lines are three-parameter fits (Q,F_{iso},λ) using the extended MG EMT [Eqs. (2)].

an extended, anisotropic form of the MG EMT [18,19]:

$$\varepsilon_{\parallel} - 1 = Q[F_{\parallel} + (\varepsilon_i - 1)^{-1}]^{-1}, \quad (2a)$$

$$1 - (\varepsilon_{\perp})^{-1} = Q[F_{\perp} + (\varepsilon_i - 1)^{-1}]^{-1}. \quad (2b)$$

Here, ∥ and ⊥ indicate directions with respect to the film plane, $\varepsilon_i(\lambda)$ is the dielectric function of the Al particles, and Q is the Al volume fraction. For the interaction parameters, $F_{\parallel}$ and $F_{\perp}$, we use the expressions of Ref. [18] that exhibit the functional form $F_j = \Im_j(Q,\gamma,\varepsilon_s)$ ($j = \parallel, \perp$), and were derived assuming (i) spheroidal particles on a square lattice and (ii) dipole-dipole interactions among particles and their images. ε_s is the substrate dielectric function (~2.17) and $\gamma \equiv b/c$ is the spheroid axial ratio, where b and c are the semiaxes parallel and perpendicular to the film.

From Eqs. (2a) and (2b), isotropy occurs for $\delta_A \equiv |F_{\parallel} - (F_{\perp} - Q)| \sim 0$. We have fitted ($\varepsilon_1$,$\varepsilon_2$) in Fig. 3 by Eq. (2a), expecting that the incident fields will be more strongly influenced by $\varepsilon_{\parallel}$, should the film be anisotropic. Quite good fits are obtained with the free parameters Q, $F_{iso} \equiv F_{\parallel}$, and λ (solid lines in Fig. 3). The results for λ and τ_{PB}, related through the expression provided above, are presented in Fig. 2 (circles). λ and τ_{PB} obtained in a corresponding analysis of the few spectra for the particle regime of the high-rate Al also appear in Fig. 2 (triangles, $d < 50$ Å).

For deduced values of F_{iso} and Q, the axial ratio can be obtained from $F_{\parallel} = \Im_{\parallel}(Q,\gamma,\varepsilon_s)$. Figure 4 shows that γ increases from 2.2 and stabilizes at 2.6 (broken lines). This result, along with the weak increase in Q, and its relatively large values, indicates that the particles are flattened and cover a large fraction of the substrate surface. The solid line in Fig. 4 is the expected behavior for spherical

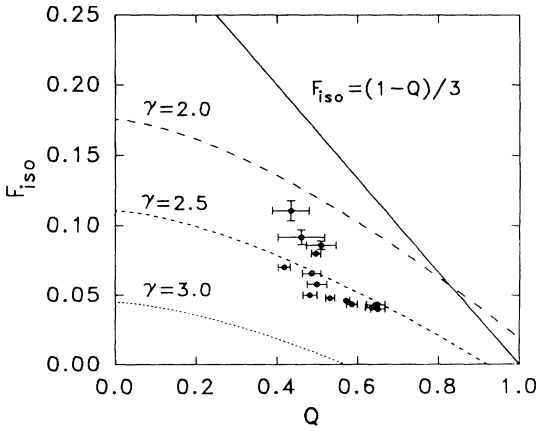

FIG. 4. Interaction parameter vs Al volume fraction obtained in the particle growth regime ($d < 50$ Å) for Al deposition (43 Å/min). Solid and broken lines are obtained for the simple (Ref. [1]) and extended (Ref. [18]) MG EMTs, respectively.

particles with the Lorentz-field interaction (simple MG), a model clearly not valid here. The complete solution of Eqs. (2) for the prescribed interaction exhibits only very weak anisotropy with $|\delta_A|$ decreasing from 0.04 to 0.003 as d increases from 10 to 50 Å. This situation results from a near-cancellation of anisotropies arising from particle shape and the dipole-dipole interaction, but is not a general feature of metal film growth, depending sensitively on the values of Q, γ, and ε_s [18]. The maximum errors in d, λ, Q, and $F_{\parallel}$ that result from assuming isotropy are within confidence limits. Finally, we note the satisfying outcome that $|\delta_A| \rightarrow 0$ as coalescence commences.

The results for λ (and τ_{PB}) in Fig. 2 for $d < 50$ Å, deduced for both high- and low-rate Al films deserve comment. First, the λ values for the low-rate Al film overlap those obtained for the high-rate film at ~ 50 Å, even though the latter is continuous. This demonstrates that λ, which controls the width of the ε_2 band in Fig. 3, is *not* artificially depressed by neglecting particle size or shape distributions. The fact that λ is nearly independent of particle size at 8 ± 2 Å for $25 < d < 50$ Å suggests that it is dominated by scattering events *internal to the particles*. This in turn suggests a highly defective, disordered, or possibly even amorphous arrangement of Al atoms in the particles. Thus, the classical size effect, with λ replaced by a particle dimension (e.g., solid line in Fig. 2 for $d < 50$ Å), used widely to interpret the optical properties of particle films, is not generally valid.

In summary, we have determined the optical functions of Al films throughout the regimes of nucleation, coalescence, and bulk growth. In the particle regime, the effective optical functions can be fitted with an extended MG EMT which includes dipole-dipole interactions between oblate nuclei. We find that the electron mean free path λ is nearly constant ($\sim$6–10 Å) even as the nuclei increase in size to a thickness of 50 Å. This suggests that scattering within the particles dominates and that λ controls the plasmon-polariton bandwidth independently of the particle size distribution. λ remains constant even as the continuous film regime is entered ($d \sim 50$ Å, for optimum conditions). Shortly thereafter, however, λ shows an abrupt transition, increasing by 1 order ($55 < d < 60$ Å). This is attributed to the healing (crystallization) of defective (disordered) domains which are the vestiges of initial nucleation. Only after this transition is the (200) parallel-band feature observed, and the evolving optical functions then reveal changes in the grain size.

Funding from the National Science Foundation (under Grant No. DMR-8957159), Philips-DuPont Optical Company, and the DuPont Corporation is gratefully acknowledged.

[1] J. C. Maxwell-Garnett, Philos. Trans. R. Soc. London A **203**, 385 (1904).
[2] L. Genzel and T. P. Martin, Surf. Sci. **34**, 33 (1973).
[3] S. Norrman, T. Andersson, C. G. Granqvist, and O. Hunderi, Phys. Rev. B **18**, 674 (1978).
[4] G. Rasigni and P. Rouard, J. Opt. Soc. Am. **53**, 604 (1963).
[5] D. A. G. Bruggeman, Ann. Phys. (Leipzig) **24**, 636 (1935).
[6] Y. Yagil and G. Deutscher, Appl. Phys. Lett. **52**, 373 (1988).
[7] D. E. Aspnes, E. Kinsbron, and D. D. Bacon, Phys. Rev. B **21**, 3290 (1980).
[8] D. E. Aspnes, Proc. Photo-Opt. Instrum. Eng. **276**, 188 (1981).
[9] N. W. Ashcroft and K. Sturm, Phys. Rev. B **3**, 1898 (1971).
[10] J. H. Halford, F. K. Chin, and J. E. Norman, J. Opt. Soc. Am. **63**, 786 (1973).
[11] I. An and R. W. Collins, Rev. Sci. Instrum. **62**, 1904 (1991).
[12] E. Shiles, T. Sasaki, M. Inokuti, and D. Y. Smith, Phys. Rev. B **22**, 1612 (1980).
[13] A. G. Mathewson and H.P. Myers, J. Phys. F **2**, 403 (1972).
[14] H. Arwin and D. E. Aspnes, Thin Solid Films **113**, 101 (1984).
[15] U. Kreibig and C. v. Fragstein, Z. Phys. **224**, 307 (1969).
[16] A. F. Mayadas and M. Shatzkes, Phys. Rev. B **1**, 1382 (1970).
[17] G. A. Niklasson, D. E. Aspnes, and H. G. Craighead, Phys. Rev. B **33**, 5363 (1986).
[18] T. Yamaguchi, S. Yoshida, and A. Kinbara, J. Opt. Soc. Am. **64**, 1563 (1974).
[19] D. Bedeaux and J. Vlieger, Physica (Utrecht) **73**, 287 (1974).